ADVANCED FUNCTIONAL MATERIALS
www.afm-journal.de

Tungsten's Role in Enhancing Sintering Resistance of Fe-W Hierarchical Foams during Redox Cycling

Ming Chen, Samuel Pennell, and David C. Dunand**

Directional freeze-cast Fe-W lamellar foams with 10–33 at.% W show distinct microstructural evolutions during steam/hydrogen redox cycling between oxidized and reduced states at 800 ^{0}C, depending on W concentration. The Fe-18 W and Fe-25 W foams exhibit a sufficient volume fraction of W-rich phases – λ-Fe_2W to inhibit sintering for α-Fe in the reduced state and $FeWO_4$ to inhibit sintering for Fe_3O_4 in the oxidized state – thus forming ligaments comprising two phases (Fe/λ-Fe_2W and Fe_3O_4/$FeWO_4$, respectively). In contrast, a Fe-10 W foam with a lower volume fraction of W-containing phases (λ-Fe_2W and $FeWO_4$) shows lamellae densification as well as core-shell structure formation, due to Fe outward diffusion during oxidation. While higher W concentration enhances the stability of lamellar structure in Fe-W foams, degradation still occurs, via buckling of lamellae and swelling of foams after extensive cycling. In situ XRD characterization shows that W addition has a minor effect on the oxidation process but slows reduction due to the sluggish kinetics of $FeWO_4$ reduction. This influence is mitigated by the formation of nanocrystalline W-rich phases due to the chemical vapor transport (CVT) mechanism during the reduction of $FeWO_4$ to boost the reaction kinetics during redox cycling.

1. Introduction

Iron – as an abundant, low-cost, and non-toxic element – is attracting enormous attention for its promising applications as an energy storage material. At elevated temperatures, iron is oxidized by steam (H_2O) exothermically, releasing hydrogen. Conversely, iron oxides can be reduced by hydrogen (H_2) to metallic iron effectively, at temperatures as low as 576 ^{0}C.[1,2] Therefore, iron can be used as an efficient energy carrier, with much higher volumetric energy density, in contrast to lithium-ion batteries and fossil fuel.[3] A representative example is the application of porous iron as energy storage material in rechargeable oxide batteries (ROB), comprising a reversible solid oxide cell (SOC) and a Fe-based energy storage unit, for grid-level energy storage and release.[4–7] In ROB, Fe powder beds in the energy storage unit are oxidized by steam to generate H_2 which is provided as fuel into SOC (fuel cell mode) during discharging; during subsequent charging in SOC (electrolyzer mode), steam is split into O^{2-} and H_2 which is then used for Fe_3O_4 reduction. In other gas-reforming technologies (e.g., chemical looping combustion,[8–13] carbon utilization,[14–16] solar thermal redox,[17] Fe and other metals act as oxygen carriers[18] to participate in similar reversible oxidation and reduction processes over multiple cycles. The key feature of these technologies is that cycled energy carrier materials, cyclically converting between metallic and oxide phases by redox reactions, need to sustain high reactivity and stable performance over numerous high-temperature redox cycles.

However, the capacity of ROB drops notably after the first several cycles, e.g., to 65% after the first ten cycles during redox cycling at 500–800 ^{0}C.[4,19,20] This is attributed to the rapid sintering of Fe and Fe_3O_4 phases at elevated temperatures, closing porosity, and decreasing free surface area, leading to very slow reaction kinetics. Moreover, the sintered structures also block gas accesses for inner materials to participate in redox cycling, decreasing redox capacity. To suppress undesirable sintering and resist structural degradation, inactive oxides, (e.g., yttria-stabilized zirconia (YSZ),[7] SiO_2,[21] $MgAl_2O_4$,[12] CeO_2, ZrO_2, Al_2O_3)[22] can be added as a support to prevent the contacting and sintering of Fe particles, without participating in the redox reactions. For example, Chung et al., added TiO_2 to Fe beds to act as a scaffold and join the reaction partially by forming $FeTiO_3$ during oxidation to suppress sintering and even increasing porosity after extensive cycling.[23]

Another strategy to enhance the structural stability of cycled materials is to combine alloying composition design with porous structure architecture to create degradation-resistant Fe-based foams instead of powder beds. 3D printing of foams creates hierarchical porous structures of Fe-based alloys for high-temperature redox cycling.[24,25] Directional freeze casting[26–30] integrated with controlled sintering demonstrates an efficient and scalable method to fabricate Fe foams with lamellar

M. Chen, S. Pennell, D. C. Dunand
Department of Materials Science & Engineering
Northwestern University
2,220 Campus Drive, Cook 2036, Evanston, IL 60208, USA
E-mail: ming.chen@northwestern.edu; dunand@northwestern.edu

The ORCID identification number(s) for the author(s) of this article can be found under https://doi.org/10.1002/adfm.202411085

DOI: 10.1002/adfm.202411085

structures, displaying directional channels, high porosity (≈62%), and low tortuosity for redox cycling.[31]

To prevent lamellar sintering and to stabilize porous structures during high-temperature redox cycling, the compositions of Fe-based foams can be further optimized. Depending on their reactivity during redox reactions, alloying elements are sorted into three categories: inactive metals, inactive oxides, and redox-active elements. Inactive metals, e.g., Cu, Co,[32] and Ni,[33–35] cannot be oxidized by steam under high-temperature redox conditions according to the Ellingham diagram[36] but form metallic scaffolds as a ductile backbone to limit fracture and buckling of lamellar structures. The interface between the Fe_3O_4 oxide and the metallic scaffold accelerates reduction kinetics due to a catalytic effect of metallic phases on oxide reduction.[37] However, due to its limited solubility, Cu within lamellae cannot recombine with Fe formed at the lamellar surface after reduction, leading to a core-shell structure. The Fe shells seal the porous lamellae surface and it also leads to sintering when lamellae contact neighbors (e.g., due to buckling), thus inducing densification that decreases inter- and intra-lamellar porosity.[32] Even for Co and Ni additions which can re-alloy with Fe after reduction, sintering and densification are still observed in lamellar foams: for example, the redox capability of Fe-24Ni lamellar foams is reduced by 90% after only 30 cycles.[25]

Inactive oxides such as Al_2O_3, MgO, and CeO_2 can increase the lifetime of Fe-based redox materials during high-temperature operation but they reduce redox capacity.[38,39] Redox-active elements, i.e., refractory elements such as Mo and W, provide significant improvements in foam stability by introducing Mo- and W-rich phases which inhibit the sintering of Fe and Fe_3O_4 during reduction and oxidation respectively. For a Fe-25Mo foam,[40] lamellae sintering was suppressed even after 50 cycles. The Mo loss was found due to the volatilization of the $MoO_2(OH)_2$ phase during reduction via a chemical vapor transport (CVT) mechanism.[41] By contrast, Fe-25 W and Fe-20Ni-20 W lamellar foams exhibit excellent resistance to degradation during redox cycling at 800 ^{0}C, without segregation and loss of W as compared to Fe-Mo foams.[42,43] This is attributed to the formation of sintering inhibitors – λ-Fe_2W during reduction and $FeWO_4$ during oxidation – which help preserve the porous structures of lamellae.

However, an investigation of the effect of W concentration (and thus the volume fraction of W-rich phases) on the sintering behavior of Fe-W foams during high-temperature redox cycling is still missing. In this work, we investigate the role of W concentration on the structural evolution of Fe-W foams during high-temperature redox cycling, by varying the W concentration from 10 to 33 at.% compared to a single composition of Fe-25 W in the previous study.[42] This introduces different volume fractions of W-rich phases (λ-Fe_2W and $FeWO_4$) acting as sintering inhibitors in the reduced and oxidized states during redox cycling, thus revealing the critical roles of W concentration on foam degradation. In situ XRD measurements are performed on Fe-10 W, Fe-18 W, and Fe-33 W to understand the effect of W concentration on redox kinetics. The structures of low- and high-W foams after various cycles are characterized from micro- to macroscale to reveal the distinct evolution processes during redox cycling with steam and hydrogen at 800 ^{0}C. The mechanisms of different evolution processes of lamellae structures in low- and high-W foams are compared to assess the impact of W concentration on the sintering resistance of foams. A compositional window for designing Fe-W foams with high degradation resistance is suggested, enabling Fe-based foams for long-term redox cycling for energy storage.

2. Results and Discussion

2.1. Phase Evolution and Thermodynamics During Redox Cycling

2.1.1. Initial Phases

The tungsten concentration in foams was varied in a range of 10–33 at.%, i.e., Fe-10 W, Fe-18 W, Fe-25 W, and Fe-33 W (vertical dashed lines in **Figure 1a**), to increase mole fractions of the intermetallic phase λ-Fe_2W from 12.5 to 100%. The Fe-W foams were sintered at various temperatures between 1000 and 1200 ^{0}C for different times, depending on W concentrations (**Table 1**). This was done to achieve similar mechanical strength and similar inter- and intra-lamellar porosity in the initial state for each foam composition. From the XRD patterns of as-sintered foams (Figure 1b), the main phases are identified as bcc α-Fe (with 1.3 at.% W in solid solution) and λ-Fe_2W, except for the Fe-25 W foam sintered at 1200 ^{0}C, for which the μ-Fe_7W_6 phase is present, consistent with the phase diagram (Figure 1a). In the Fe-33 W foam with a stoichiometry of Fe:W = 2:1, the α-Fe, λ-Fe_2W, and μ-Fe_7W_6 are observed simultaneously in the as-sintered state. The presence of α-Fe and μ-Fe_7W_6 phase indicates that the formation of λ-Fe_2W phase is incomplete with the current sintering profiles, i.e., 7 h at 1000 ^{0}C, in the α-Fe + λ-Fe_2W field below the peritectic temperature of 1060 ^{0}C. This might be attributed to the sluggish diffusion of Fe and W atoms in Fe-W foams with a highly porous structure. Increasing the sintering temperature and extending the sintering time can promote diffusion and reaction to form a complete λ-Fe_2W structure, i.e., $Fe_7W_6 + 5Fe \rightarrow 6Fe_2W$. However, increasing sintering time may eliminate porous structures and decrease the kinetics of redox cycling. In our preliminary study of Fe-25 W foams,[42] μ-Fe_7W_6 is entirely converted into λ-Fe_2W, a thermally stable phase (Figure 1a), after the first redox cycle at 800 ^{0}C. In all Fe-W foams with varying W concentrations, α-Fe and λ-Fe_2W remain the primary phases involved in oxidation during redox cycling.

2.1.2. Phase Evolution During Redox Cycling

In as-sintered foams with various W concentrations (i.e., Fe-10 W, Fe-18 W, and Fe-33 W), the evolution of XRD patterns as a function of time in the first redox cycle is plotted in **Figures 2a**, **3a**, and **4a** respectively, labeling each phase. The corresponding normalized peak intensities of both metallic and oxide phases were determined as a function of reaction time to demonstrate phase evolution semi-quantitatively. During the oxidation stage, the initial phases (α-Fe and λ-Fe_2W in Fe-10 W and Fe-18 W foams) are oxidized to FeO, Fe_3O_4, and $FeWO_4$. According to the evolution of normalized intensity, $FeWO_4$ forms first, followed by FeO and then Fe_3O_4 in the first 10 mins (Figures 2c and 3c). The intensity of FeO rises before declining as the Fe_3O_4 intensity increases, suggesting an oxidation sequence as $Fe \rightarrow FeO \rightarrow Fe_3O_4$. This result is consistent with the calculated ternary Fe-W-O phase diagram at 800 ^{0}C and in situ XRD findings in a previous study of

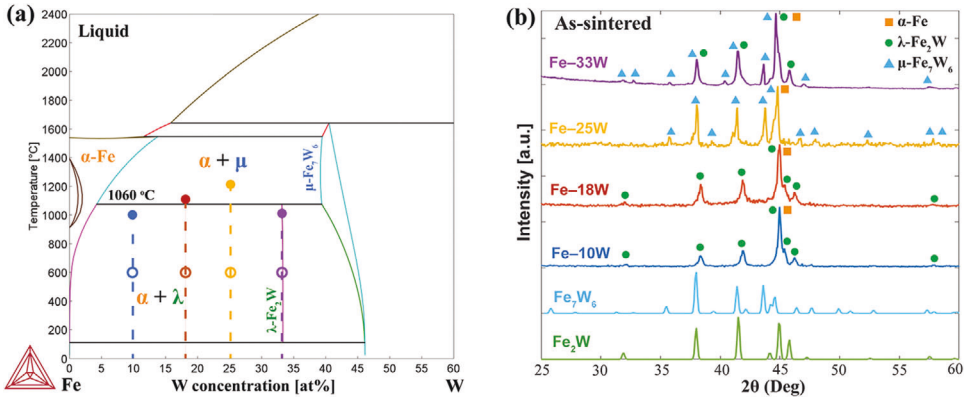

Figure 1. a) Fe-W phase diagram from CALPHAD-based calculation using Thermo-Cal software, showing compositions of the four Fe-W foams at their reduction temperature of 600 °C (hollow symbols) and at their subsequent sintering temperatures (1000, 1100, and 1200 °C, solid symbols). b) X-ray diffraction patterns of as-sintered Fe-W foams, with phases identified. The reported diffraction patterns of Fe_7W_6[44] and Fe_2W[45] phases are plotted as well.

freeze-cast Fe-25 W.[42] The thermally stable Fe_3O_4 and $FeWO_4$ phases achieve their maximum intensities after oxidation for 20 mins. Although μ-Fe_7W_6 is initially present in the as-sintered Fe-33 W foams (Figure 4b), the oxidation behavior is similar to other foams with different W concentrations.

During the reduction stage, the reduction of Fe_3O_4 progresses as Fe_3O_4 → FeO → Fe in the first 20–25 min. The intensity of FeO diffraction peaks first increases and then drops quickly and disappears, indicating fast reduction to Fe, as shown in Figure 2c. The FeO → Fe reduction kinetics by hydrogen at 700 ^{0}C are typically slower than the Fe_3O_4 → FeO reduction step, due to the sluggish outward diffusion of oxygen through a dense Fe shell.[46,47] The fast reduction of FeO in the present foam can be attributed to the higher reduction temperature of 800 ^{0}C and highly porous

Table 1. Precursor volume fraction in suspensions and peak sintering profiles for the four Fe-W foams studied.

Foam [at%]	Fe_2O_3 [vol%]	WO_3 [vol%]	DI Water [vol%]	Zephrym [vol%]	Polyethylene glycol [vol%]	Peak sintering
Fe-10W	8.08	1.92	87.49	0.51	2.00	1000 °C /3.5 h
Fe-18W	6.81	3.18	87.48	0.53	”	1100 °C/3.5 h
Fe-25W	5.84	4.15	87.46	0.55	”	1200 °C/3.5 h
Fe-33W	4.87	5.12	87.45	0.57	”	1000 °C/7.0 h

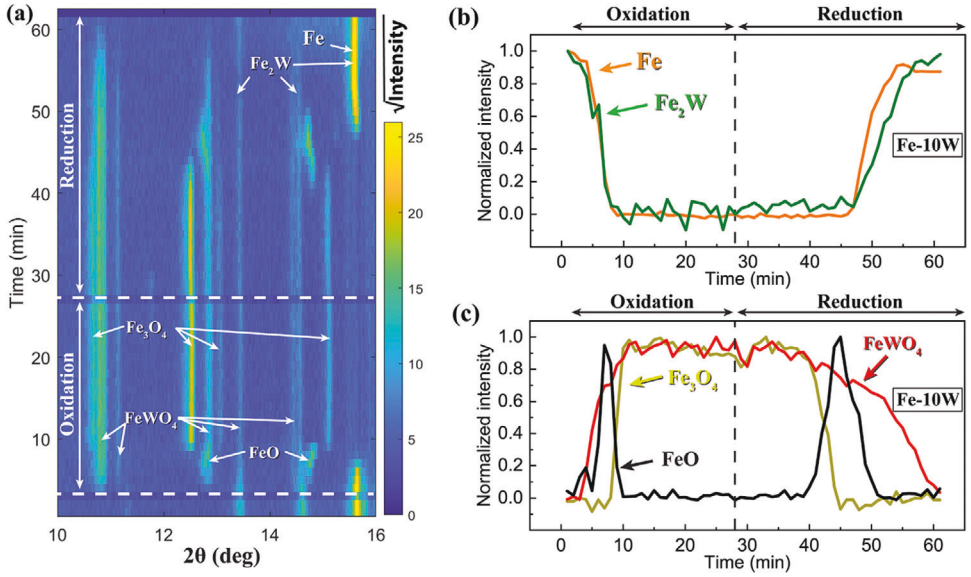

Figure 2. In situ XRD characterization of Fe-10 W foam during the first redox cycling at 800 ^{0}C. a) Evolution of XRD patterns as a function of time for the first oxidation/reduction cycle. b,c) Evolution of normalized peak intensity integrals during the first oxidation/reduction cycle for (b) metallic phases and (c) oxide phases.

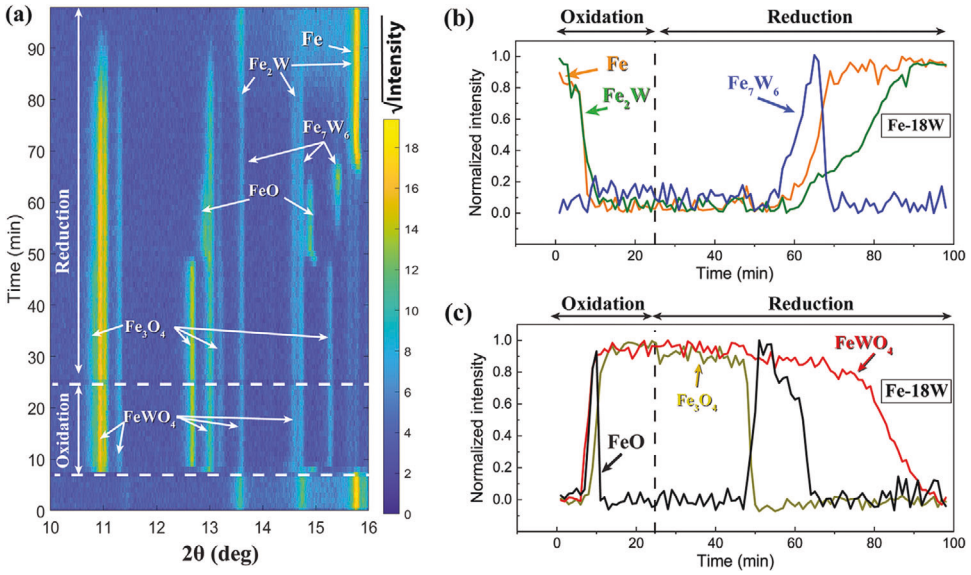

Figure 3. In situ XRD characterization of Fe-18 W foam during the first redox cycling at 800 ^{0}C. a) Evolution of XRD patterns as a function of time for the first oxidation/reduction cycle. b,c) Evolution of normalized peak intensity integrals during the first oxidation/reduction cycle for (b) metallic phases and (c) oxide phases.

structures with a large surface area.[2] As a comparison, the necessary time for complete reduction of $FeWO_4$ spans from 30 min in Fe-10 W foam (Figure 2c) to 75 min in Fe-33 W foam (Figure 4c). This indicates faster reduction kinetics of Fe_3O_4 than the more stable $FeWO_4$, which needs much longer time for complete reduction, especially in foams with higher W concentration (due to a higher volume fraction of $FeWO_4$ formed). In Fe-10W foam (Figure 2b), the two reduction products, α-Fe and λ-Fe_2W, form and grow with similar kinetics. During the reduction of Fe-18 W (Figure 3b) and Fe-33 W (Figure 4b) foams, the μ-Fe_7W_6 is observed as a transient, non-equilibrium phase before the equilibrium λ-Fe_2W phase forms. The λ-Fe_2W intensity increases gradually with the decline of μ-Fe_7W_6 intensity, suggesting the reaction of $Fe_7W_6 + 5Fe \rightarrow 6Fe_2W$. In Fe-33 W foam (Fe:W = 2:1), both μ-Fe_7W_6 and α-Fe phases first form on reduction, but are then depleted to form a single phase λ-Fe_2W after reduction for sufficiently long times (≈75 min). The complete reduction of Fe-W foam with higher W concentrations is much longer due to the slow reduction kinetics of $FeWO_4$. During reduction, the presence of the transient phase μ-Fe_7W_6, which is thermally unstable at 800 ^{0}C according to the calculated Fe-W phase diagram (Figure 1a), prior to λ-Fe_2W indicates a gradual alloying process

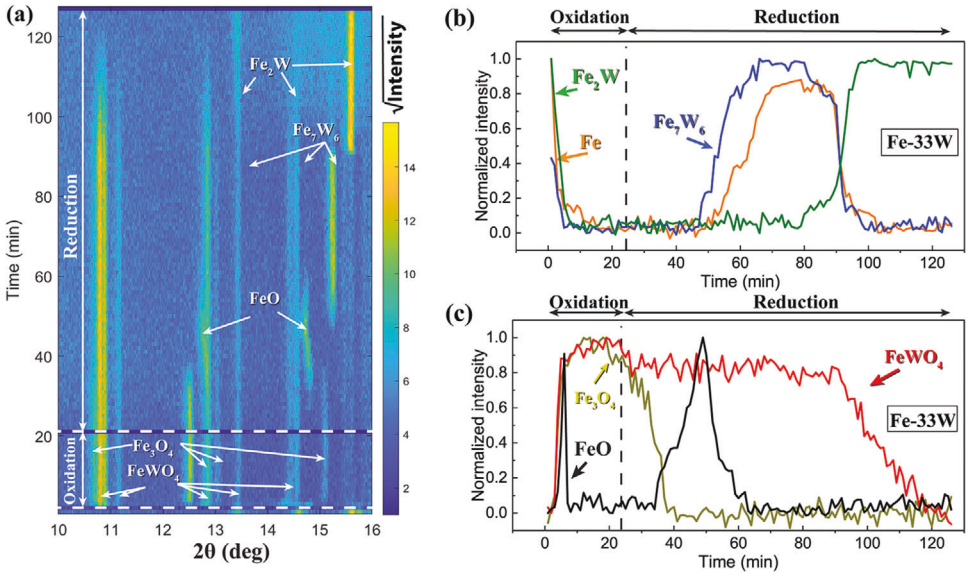

Figure 4. In situ XRD characterization of Fe-33 W foam during the first redox cycling at 800 ^{0}C. a) Evolution of XRD patterns as a function of time for the first oxidation/reduction cycle. b,c) Evolution of normalized peak intensity integrals during the first oxidation/reduction cycle for (b) metallic phases and (c) oxide phases.

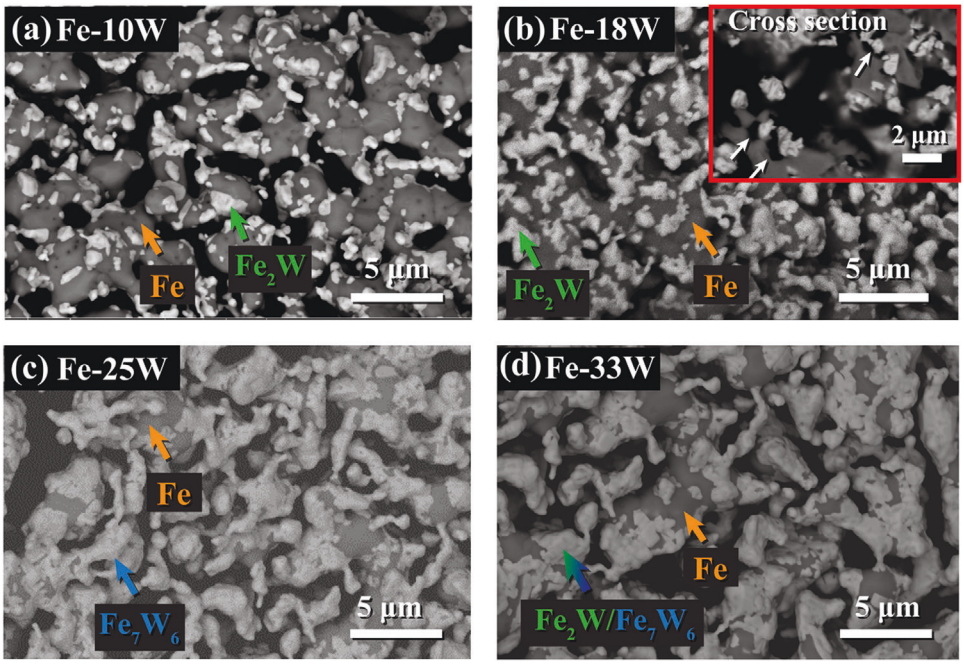

Figure 5. Backscattered electron (BSE) micrographs of lamellar surface in the Fe-W foams: a) Fe-10 W, b) Fe-18 W, c) Fe-25 W, and d) Fe-33 W. The α-Fe, λ-Fe_2W, and μ-Fe_7W_6 phases are marked in each foam, and micropores have black contrast. Submicron porosities in the cross-section view of Fe-18 W foam are marked with white arrows in the higher-magnification insert in (b).

of Fe with W to form the thermally stable λ-Fe_2W. The μ-Fe_7W_6 is not observed in Fe-10 W during the reduction process (Figure 2b). Its intensity might be too low to be detected due to the relatively lower W concentration.

2.1.3. Thermodynamic Consideration of Fe-W Foams

During redox cycling at 800 ^{0}C, Fe and λ-Fe_2W phases are stable in the reduced state and Fe_3O_4 and $FeWO_4$ are stable in the oxidized state. The corresponding redox reactions and associated ions and electrons exchange follow the reversible reactions below:

$$3Fe + 4H_2O \leftrightarrow Fe_3O_4 + 4H_2 \quad (1)$$

$$4H_2O \leftrightarrow 4H_2 + 4O^{2-} + 8e^- \quad (2)$$

$$Fe_2W + \frac{16}{3}H_2O \leftrightarrow FeWO_4 + \frac{1}{3}Fe_3O_4 + \frac{16}{3}H_2 \quad (3)$$

$$\frac{16}{3}H_2O \leftrightarrow \frac{16}{3}H_2 + \frac{16}{3}O^{2-} + \frac{32}{3}e^- \quad (4)$$

progressing forward under steam (H_2O) oxidation and backward under H_2 reduction. In the context of ROB operation, steam oxidation corresponds to energy discharge, and H_2 reduction corresponds to energy recharge. The reaction Equations (1) and (3) show that the metallic phases in foams are oxidized in the discharging mode by capturing oxygen and then reduced in the charging mode by releasing oxygen in metal-air batteries.[4] The reaction Equation (3) also indicates the participation of W in redox cycling by forming W-rich phases, i.e., λ-Fe_2W in the reduced state and $FeWO_4$ in the oxidized state, which prevents W segregation.

From an electrochemical perspective, electrons are exchanged between hydrogen ions and molecules during discharge and charge processes, as illustrated in Equations (2) and (4). For 1 mole of Fe and W atoms, both oxygen and hydrogen capacities increase linearly as W concentration increases from 0 to 33 at.%, with oxygen increasing from 1.33 to 1.77 mol and hydrogen increasing from 2.67 to 3.55 mol, as plotted in Figure S1a,b (Supporting Information). However, due to the high mass density of W, the oxygen capacity per alloy unit mass decreases near linearly, from 382 to 289 g kg^{-1} (a 24% drop), with a concomitant decrease in hydrogen capacity per alloy unit mass, from 47.8 to 36.2 g kg^{-1} (a 24% drop). The electron numbers, which are proportional to the charge capacity, increase from 2.57 to 3.40×10^5 C as W concentration increases from 0 to 33 at.% in the alloy. The theoretical Nerst potentials (E_N) of Fe-W foams, calculated using equations reported in Ref,[42] show a slight decrease from 0.94 to 0.92 V with increasing W (Figure S1c, Supporting Information), indicating a negligible effect of W concentration on the theoretical battery voltage for an ROB using Fe-W foams as the energy storage material.

2.2. Microstructural Evolution During Redox Cycling

2.2.1. Initial Microstructures in as-Sintered Foams

Figure 5 shows the surface of lamellae in Fe-W foams with various W concentrations after reduction and sintering. To achieve sufficient mechanical strength for handling but maintain the porous microstructure for better redox cycling, Fe-W foams

were only sintered partially. Microscale sintering-inhibition pores forming a continuous network are observed at the lamellae surface. Submicron porosity between α-Fe and intermetallic phases is also visible in the cross-sections of lamellae (white arrows in an inserted view in Figure 5b). The micron- and submicron-pores, in combination with the freeze-cast channels (≈tens of microns) between lamellae (Figure S1, Supporting Information) form hierarchical porosity in the freeze-cast foams, which provide a large amount of surface for redox reactions and easy access for H_2/steam transport, enabling fast reaction kinetics. As-sintered Fe-10 W, Fe-18 W, and Fe-25 W after peak sintering in a temperature range of 1000–1200 °C for 3.5 h have surface areas of 1.7, 2.2, and 6.7 $m^2\ g^{-1}$ respectively according to the Brunauer–Emmett–Teller (BET) measurements. The porosity thus increases with higher W concentration, consistent with the sintering inhabitation effect of W.[42] The preservation of such hierarchical porous structures during high-temperature redox cycling is crucial for prolonging cycling durability and sustaining the charging capacity of rechargeable oxide batteries for a long lifespan.

The intermetallic phases – λ-Fe_2W and μ-Fe_7W_6 with sizes of 2–3 μm, with brighter contrast due to W in BSE micrographs – are evenly mixed with the α-Fe phase in as-sintered foams. With increasing W concentration from 10 to 33 at.%, the volume fraction of the intermetallic phase increases, as expected. Moreover, the morphology of the intermetallic phase transitions from isolated particles in Fe-10 W foam (Figure 5a) to a 3D network in foams with higher W concentration (Figure 5b–d). In Fe-33 W foam, α-Fe is also observed to distribute randomly between intermetallic μ-Fe_7W_6 and λ-Fe_2W phases, consistent with XRD measurement (Figure 1b), due to insufficient time for diffusion to form a complete λ-Fe_2W structure during the sintering process. However, it is difficult to differentiate μ-Fe_7W_6 and λ-Fe_2W phases in BSE contrast due to a relatively small difference of W concentrations between the two phases. The SE micrographs of an identical region on the lamellae surface also show no difference in grain morphologies between both the W-rich phases (Figure S2, Supporting Information). According to the in situ XRD characterization (Figure 4b), μ-Fe_7W_6 is converted to λ-Fe_2W, a thermally-stable phase during redox cycling at 800 ^{0}C, after the first cycle.

2.2.2. Microstructural Evolution

The evolution of the lamellar structures during redox cycling was investigated by inspecting microstructures after reduction and oxidation for different cycle numbers in Fe-10 W, Fe-18 W, and Fe-25 W foams. The Fe-33 W foams are not investigated since the high faction of λ-Fe_2W requires a long reduction time (≈75 min, Figure 4c). **Figure 6** shows radial cross-sections of the three foams after 20 redox cycles. The lamellae in Fe-10 W foams display a distinct core-shell structure, i.e., a dense Fe-rich shell (orange arrow) with a porous, W-rich core (Figure 6a,b), in contrast to homogenous porous structures exhibited by lamellae in Fe-18 W and Fe-25 W foams. This core-shell structure is not present in the lamellae of Fe-10 W foams in the as-reduced state, comprising a homogeneous mixture of α-Fe with λ-Fe_2W phases (Figure 5a), before redox cycling. The result indicates, in Fe-10 W during redox cycling, a strong outward diffusion of Fe toward the lamellar surface from the lamellar core, resulting in a highly porous core. In contrast, the α-Fe with λ-Fe_2W phases are observed to mix homogeneously and form ligaments with sizes of 3–5 μm (red dashed circle in Figure 6d) in Fe-18 W and Fe-25 W foams after 20 cycles. These ligaments connect with neighboring ligaments to form a 3D-interpenetrating network of α-Fe with λ-Fe_2W. The α-Fe and λ-Fe_2W phases are much finer in size for foams after 20 cycles compared to as-sintered foams (Figure 5). Moreover, the channels between lamellae in Fe-10 W after 20 cycles are much narrower compared to those in Fe-18 W and Fe-25 W foams, implying higher sintering and densification in Fe-W foams with lower W concentration.

To understand the evolution process of Fe-10 W foams during redox cycling, the lamellar microstructures are shown in **Figure 7** after 1 and 20 cycles in the oxidation state. After the first cycle, Fe_3O_4 (yellow arrow) and $FeWO_4$ (red arrow) phases are mixed throughout the lamellae (Figure 7a,b). The α-Fe oxidation (Fe → Fe_3O_4) induces a notable molar volume expansion (≈110%) which fills the microporosity widely distributed within the as-sintered foams (Figure 5a). The $FeWO_4$ phase (with higher brightness in BSE micrographs) is found between the faceted Fe_3O_4 phase (Figure 5b), inhibiting its contacting and sintering during oxidation. After 20 cycles, oxidized lamellae exhibit dense Fe_3O_4 shells (yellow arrows) and porous cores enriched with isolated $FeWO_4$ regions, as shown in Figure 7c. This core-shell structure indicates a gradual outward diffusion of Fe during oxidation which forms a dense shell after multiple cycles. The imbalance between the outward diffusion of Fe to the lamellar surfaces and the inward diffusion of oxygen results in Kirkendall pore formation in the lamellar core. This phenomenon was reported in previous studies of pure Fe foams, as well as Fe—Co, Fe—Cu,[32] and Fe—Ni[35] foams alloyed with redox inactive elements – unoxidized by steam under standard redox conditions – which form a metallic core encased within a Fe_3O_4 shell after oxidation. This core-shell structure is observed in both oxidized and reduced lamellae in the present Fe-10 W foams, which, at the microscopic level, undergo notable densification due to extensive contact and sintering of neighboring lamellae with pure Fe_3O_4 shells during redox cycling.[32] For instance in lamella #2, two thinner lamellae (#2a and #2b) contacted and then sintered together at the top part but left a fork at the bottom marked by a green arrow in Figure 7c. In an inclined view of oxidized lamellae (Figure 7d), cracks are observed directly on the side surface of the Fe_3O_4 shells. These through-cracks provide ingress of steam and egress of H_2 during oxidation and oxidation, respectively, in the redox cycles.

In Fe-18 W foams, a different morphology of oxidized lamellae is demonstrated, with a homogeneous mixture of Fe_3O_4 and $FeWO_4$ phases crisscrossed by microchannels observed in a cross-section view of lamellae after 1 and 20 cycles, as illustrated in **Figure 8**. Both oxides, which adhere to each other, form ligaments with neither phase separation nor core-shell structure observed after 20 cycles. After 20 cycles, the size of oxide ligaments separated by microchannels decreases to 2–5 μm, accompanied by notable refinement of the $FeWO_4$ phase to submicron size (red arrows, Figure 8b). This is attributed to a chemical vapor transport (CVT) mechanism[48–50] during $FeWO_4$ reduction which produces nanocrystalline λ-Fe_2W,[42] in which mixed oxide $FeWO_4$ decomposes to WO_x + FeO_{4-x} by forming vapor-phase $WO_2(OH)_2$, which is further reduces under flowing H_2 to

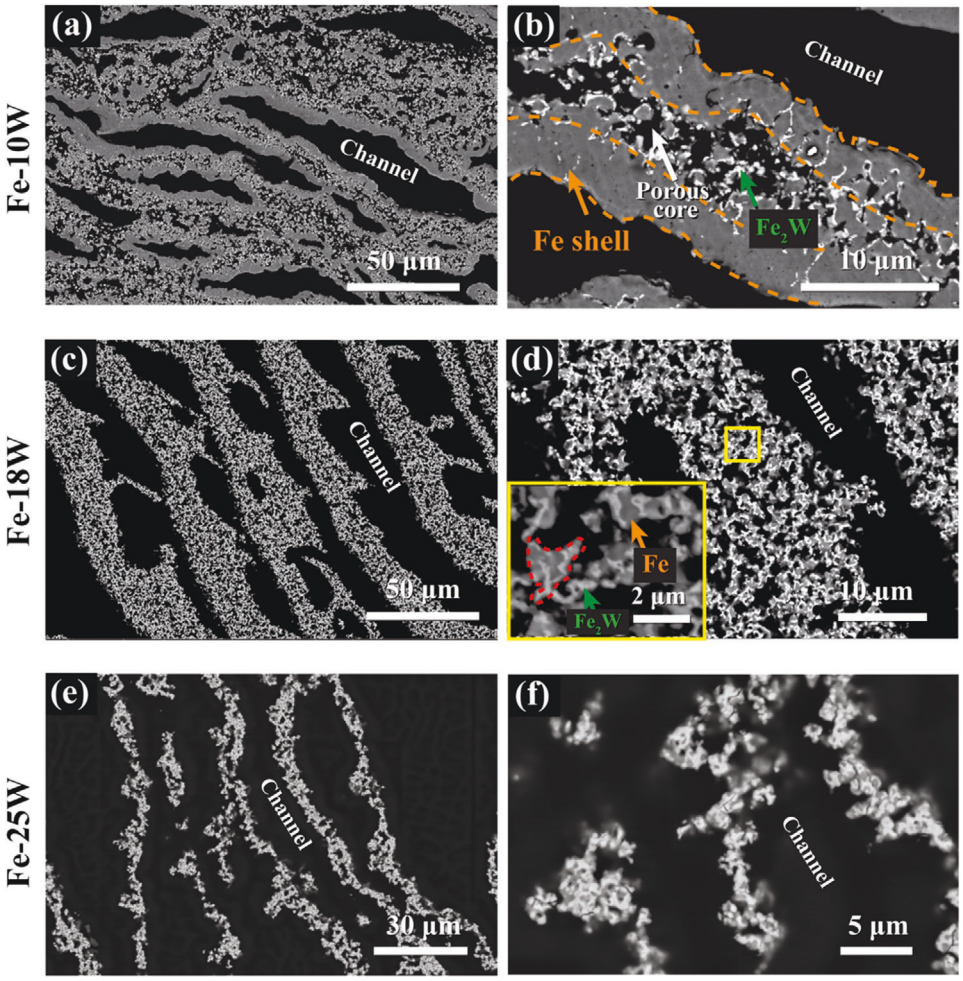

Figure 6. BSE micrographs of the cross-section of lamellar structures of a,b) Fe-10 W, c, d) Fe-18 W, and e,f) Fe-25 W foams in the reduced state after 20 redox cycles at 800 ^{0}C. A ligament within a porous lamella – consisting of α-Fe and λ-Fe_2W phases and microporosity (black contrast) – is highlighted with a red dashed circle.

metallic W, releasing H_2O. However, the W phase was not detected during the reduction of Fe-W foams by using in situ XRD characterization. A possible reason might be the quick recombination of W with surrounding Fe to form the thermally-stable λ-Fe_2W phase at 800 ^{0}C. This CVT mechanism has also been observed to induce nanocrystalline λ-Fe_2Mo in Fe-Mo foams during redox cycling.[40] The adhesion of Fe_3O_4 to the refined $FeWO_4$ within the oxidized micro-ligaments prevents phase separation and sintering of Fe_3O_4 in oxidized Fe-18 W foams. In the reduced Fe-18 W foams (Figure 6d), nanocrystalline λ-Fe_2W attached to α-Fe phase also inhibits the sintering and coarsening of the metallic micro-ligaments.

Since foams with higher W concentration display excellent resistance to phase separation and degradation of their lamellar structure in both the oxidized and reduced states, Fe-18 W and Fe-25 W foams were further subjected to 50 redox cycles to investigate their long-term microstructure evolution. **Figure 9** shows the gradual evolution of lamellar structures in Fe-18 W foams, in the reduced state, after 1, 25, 30, and 50 cycles. The left column of Figure 9 shows BSE micrographs at low magnification displaying lamellar buckling with increasing cycling numbers. The higher magnification micrographs on the right column of Figure 9 show a decrease of ligament size and increasing volume fraction of microporosity within the lamellae. The dimension of the ligaments (highlighted by red dashed circles), consisting of α-Fe and λ-Fe_2W bonded together, decreases from 5 to 10 μm after 1 cycle (Figure 9b) to 2–4 μm after 50 cycles (Figure 9h). This provides additional free surface area and decreases the diffusion distance, thus accelerating the redox reaction. The results in Fe-18 W foams are distinct from the densification of lamellae with a core-shell structure observed in Fe-10 W foams (Figure 6a) and in previous Fe-Co, Fe-Cu,[32] and Fe-Ni[35] foams as well. In a previous study of Fe-25 W foams,[42] increasing porosity in lamellae is mainly attributed to (i) the presence of sintering inhibitor λ-Fe_2W that hinders sintering at 800 ^{0}C; and (ii) the regeneration and accumulation of submicron porosity induced by the CVT mechanism during reduction. The present results in Fe-W foams with various compositions indicate that strong sintering inhibition and degradation resistance are dependent on W concentrations as well. A threshold W concentration exists between 10 and 18 at.%, which introduces a sufficiently high-volume fraction of λ-Fe_2W and $FeWO_4$ to inhibit sintering and phase separation.

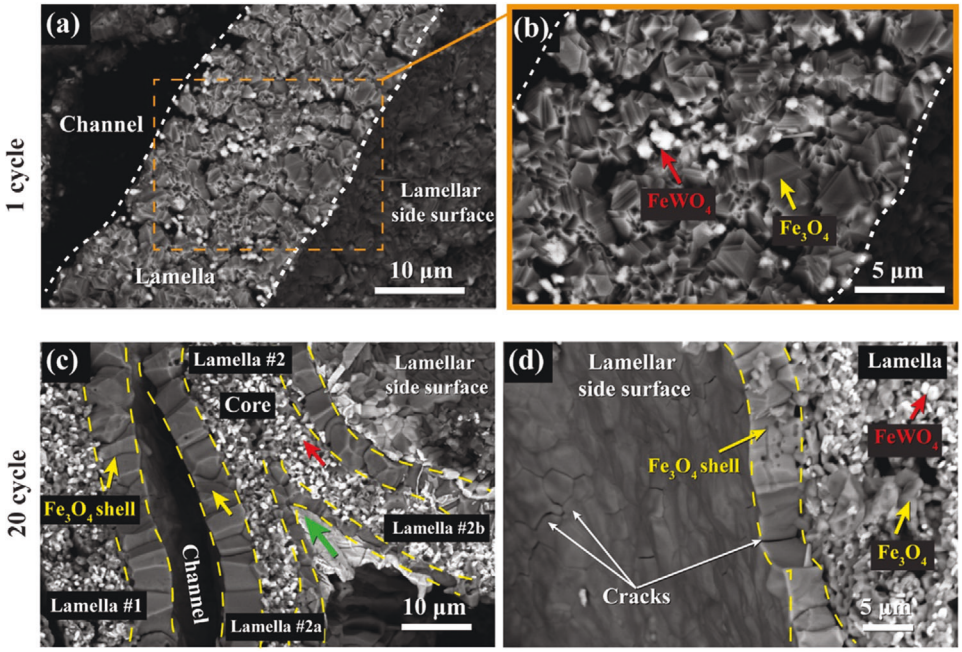

Figure 7. BSE micrographs of unmounted Fe-10 W lamellae in the oxidized state after a,b) 1 redox cycle and c,d) 20 redox cycles at 800 ^{0}C. (a) Cross-section of an oxidized lamella after the first cycle; in this inclined view, the white dashed lines indicate the edges of the lamella. (b) A magnified view of the lamella cross-section in (a). (c) Cross-section of two oxidized lamellae separated by a channel, after 20 redox cycles. The yellow dashed lines show the edges of Fe_3O_4 shells formed at the lamellae surface. For lamella #2, two lamellae (#2a and #2b) contacted and sintered together on the top part but left a fork at the bottom marked with a green arrow. (d) An inclined view showing the side surface of an oxidized lamellae, with cracks in the shell providing gas access to the porous core.

The 3D interpenetrating networks of α-Fe/λ-Fe_2W in the reduced state and Fe_3O_4/$FeWO_4$ in the oxidized state appear to be crucial for lamellae to resist degradation during redox cycling.

To confirm phase composition after redox cycling, XRD patterns were collected in reduced Fe-18 W foams after 1, 25, 30, and 50 redox cycles, as shown in **Figure 10**. The results indicate that the phase composition of the cycled foams is identical to that of the as-sintered foams (Figure 1b), consisting of α-Fe and λ-Fe_2W. Notably, the (1 0 3) reflection of λ-Fe_2W changed from a sharp peak in the as-sintered state (Figure 1b) to a broad hump in the 2θ range of 40^0–44^0 (grey shaded area) after the first redox cycle, implying the presence of nanocrystalline grains. However, the sharp (1 1 0) reflection still indicates a crystalline structure for the λ-Fe_2W phase. The sharpness of (2 0 0) and (1 1 2) reflections for λ-Fe_2W, i.e., for 2θ angles of 44.1^0 and 44.9^0, are difficult to assess due to their proximity to the α-Fe (1 1 0) ($2\theta = 45^0$) reflection. The presence of both sharp peak and broad hump for the λ-Fe_2W phase might be attributed to the refinement of grain sizes or the special grain morphologies[51] after reduced cycling. According to the microstructure study, redox cycling refines the grain size of the λ-Fe_2W phase, and may lead to the co-existence of crystalline and nanocrystalline grains. This phenomenon was also reported in the hydrogen reduction of Fe_2MoO_4 to Fe_2Mo[52] and redox cycling of Fe-25 W foams.[42]

2.2.3. Macrostructural Foam Evolution

The cross-section of Fe-W foams was examined at a larger scale to assess the structural evolution of the entire foam. **Figure 11**

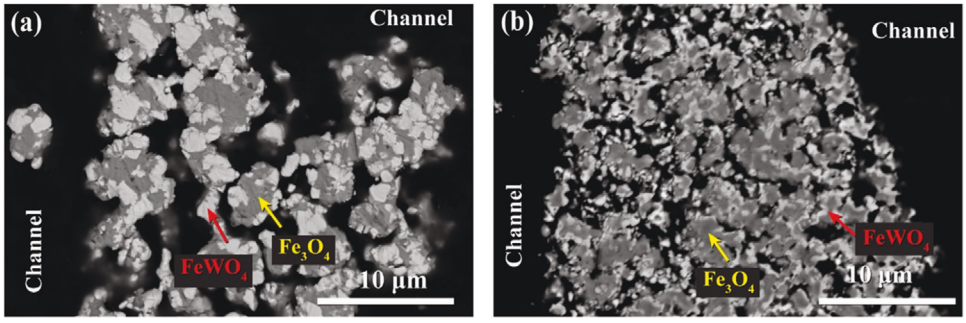

Figure 8. BSE micrographs of the cross-section of a Fe-18 W porous lamella in the oxidized state after a) 1 cycle and b) 20 cycles at 800 ^{0}C.

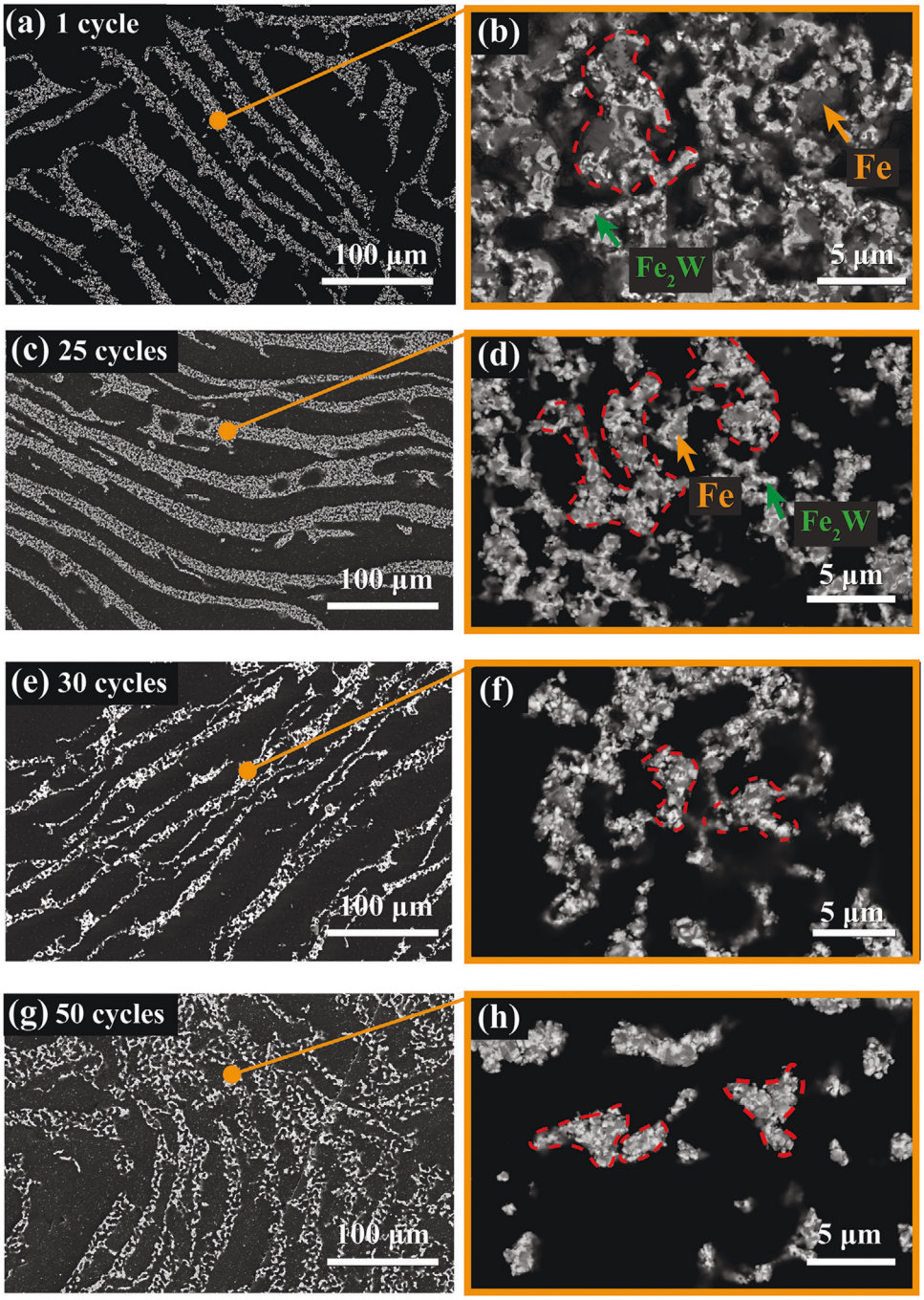

Figure 9. BSE micrographs of the cross-section of lamellar structures of Fe-18 W foams in the reduced state after a,b) 1 cycle, c,d) 25 cycles, e,f) 30 cycles, and g,h) 50 redox cycles, illustrating lamellar buckling, as well as increasing microporosity and decreasing ligament size within lamellae with increasing cycling numbers. Ligaments within a porous lamella – consisting of α-Fe and λ-Fe_2W phases and microporosity (black contrast) – are highlighted with red dashed circles.

shows a radial cross-section view at the edge of Fe-10 W foams in the reduced and oxidized states after 20 cycles, displaying the formation of a macroscale shell structure encasing the entire foam. In the reduced state (Figure 11a), sintering and densification during redox cycling are observed in Fe-10 W by the decrease in channel width and more contacts between neighboring lamellae as compared to the as-sintered foams (Figure S3a, Supporting Information). Additionally, a dense Fe shell (white dashed line), with a thickness of ≈15–20 µm, forms on the surface of the entire foam. The dense Fe macroshell decreases gas accesses (e.g., H_2 ingress and steam egress during reduction) thus affecting reaction speeds. In the oxidized state, a thicker Fe_3O_4 shell is observed on the surface of foams, as shown in Figure 11c,d. This thick Fe_3O_4 shell also hinders steam

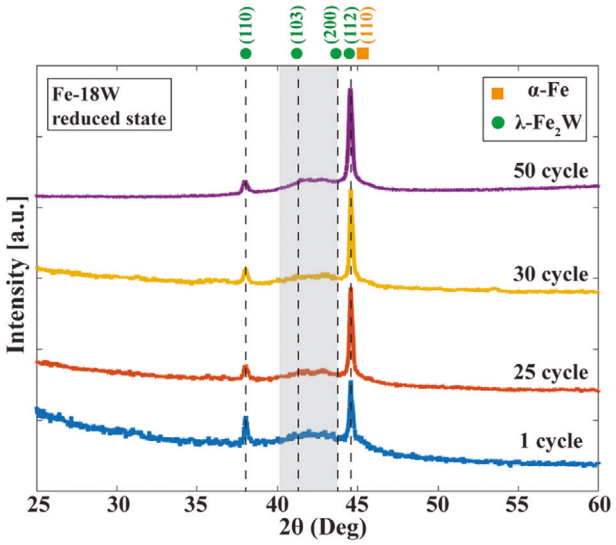

Figure 10. XRD patterns of Fe-18 W foams in their reduced, metallic state, after 1, 25, 30, and 50 redox cycles. The hump marked with a grey shadow shows strong peak broadening of the nanocrystalline λ-Fe_2W phase.

ingress and H_2 egress during the oxidation process. Thus, the core-shell structure of Fe-10 W foams at the macro-scale encapsulates the foam interior and then blocks gas channels during redox cycling, leading to sluggish reactions and decreased foam utilization.

By contrast, Fe-18 W foams demonstrate a quite different evolution of their macrostructure after 20 cycles, as shown in **Figure 12**. The axial cross-section of the entire Fe-18 W foam in the reduced state displays extensive lamellae buckling, similar to that observed in a previous study of Fe-25 W foams,[42] but without the formation of a shell encapsulating the foam, as observed in Fe-10 W. The high aspect ratio of lamellae makes them susceptible to deformation due to internal stresses caused by volumetric expansion and contraction during redox cycling. However, this deformation is constrained due to their proximity to neighboring lamellae, leading to buckling. Additionally, the strength of the lamellae is low at 800 °C, and creep deformation is likely, particularly after numerous cycles. Furthermore, increasing porosity in lamellae with cycling numbers reduces the yield strength of lamellae and induces higher degrees of plastic buckling. Lamellae buckle isotopically in both radial and axial directions, resulting in a swelling of the foams. Notably, the buckled lamellae at the bottom of the foam (yellow dotted frame) are extensively deflected in the radial direction (blue arrows), characterized as a brooming deformation at the bottom of the foam, most probably due to gravity. In the center of foam marked by a white dashed circle, buckled lamellae contact with their neighbors extensively, resulting in sintering and gradual loss of lamellar structure after long-term cycling.

2.3. Degradation Mechanisms of Fe-W Foams

Although adding tungsten, a strong sintering inhibitor, to Fe foams improves the stability of the lamellar structure by reducing lamellae sintering and densification, the core-shell structure at both micro- and macro-scale levels is still observed in Fe-10 W foams after 20 cycles. In contrast, Fe-18 W and Fe-25 W foams are more stable, forming a 3D network of binary phase ligaments (α-Fe/λ-Fe_2W in the reduced state and Fe_3O_4/$FeWO_4$ in the oxidized state), even after 50 cycles. This is consistent with the observation in our preliminary studies in Fe-25 W and Fe-20Ni-20 W foams made by the same freeze-casting process.[42,43] The result demonstrates a crucial role of W concentration and the associated effect in preventing structural degradation after extensive cycles number. The detailed mechanism is illustrated through a series of cross-sectional sketches of lamellae in foams with two W concentrations during redox cycling, as shown in **Figure 13**. In the low-W foams, α-Fe and λ-Fe_2W phases are mixed homogeneously in the as-sintered lamellae initial microstructure (Figure 13b). The phase separation between Fe_3O_4 and $FeWO_4$, leading to a core-shell structure, is illustrated in the oxidized lamellae after several redox cycles (Figure 13c). As Fe diffuses outward to the lamellar surface, a dense Fe_3O_4 shell forms, encasing each lamella and decreasing their surface during oxidation at 800 ^{0}C. After reduction, the shell structure in lamellae is preserved (Figure 13d), inducing sintering and densification of neighboring lamellae.

In the high-W foams, a larger volume fraction of λ-Fe_2W is mixed within the α-Fe phase to form a 3D interpenetrating network, as depicted in Figure 13e. The adhesion between both phases suppresses the outward diffusion of Fe during oxidation and prevents the formation of detrimental core-shell structure in the oxidized state, as sketched in Figure 13f. Additionally, the $FeWO_4$ phase acts as a sintering inhibitor by separating Fe_3O_4 particles and suppressing their sintering during oxidation. After reduction, the contact between the α-Fe and λ-Fe_2W phases, forming ligament structures within each lamella, also hinders phase separation in the metallic state (Figure 13g). Thus, W addition (>10 at.%) enhances the stability of Fe lamellar structures effectively at two levels: (i) atomic-scale bonding of Fe and W, i.e., formation of λ-Fe_2W and $FeWO_4$ in the reduced and oxidized states respectively, to prevent W segregation; (ii) micro-scale mixture of α-Fe/λ-Fe_2W in the reduced state and Fe_3O_4/$FeWO_4$ in the oxidized state to form ligaments and thus suppress phase separation and associated densification. In the early attempts to use Fe powder beds in ROB, rapid sintering of Fe and Fe_3O_4 phases at elevated temperatures (500–800 ^{0}C) resulted in a fast drop of the battery capacity to 65% after ten cycles.[4,19,20] The present Fe-18 W and Fe-25 W foams, due to their enhanced resistance to sintering and fast reaction kinetics during redox cycling at 800 °C, are promising for the applications as energy storage materials in ROB for high-cycling energy storage with a long lifespan. Furthermore, Fe-W foams with stable porous structures during high-temperature redox cycling can be used in other gas-reforming technologies, e.g., chemical looping combustion,[8–13] carbon utilization,[14–16] and solar thermal redox.[17]

However, lamellar evolution is still observed after extensive cycling in both Fe-18 W and Fe-25W foams as a strong refinement of ligament sizes and as lamellar buckling. Specifically, in Fe-25 W foams, the lamellar structure evolves into near-isotropic, highly-porous, powder network, as shown in both cross-section and surface views (Figure S4, Supporting Information) after 50 cycles. The CVT mechanism during the reduction and

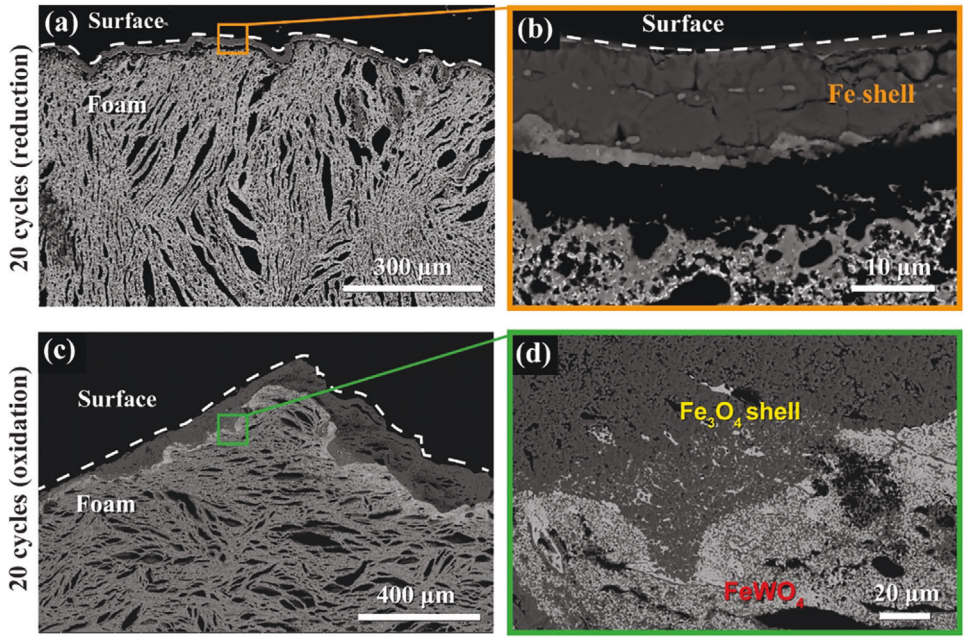

Figure 11. BSE micrographs of the radial cross-section at the edge of Fe-10 W foams, showing shell formation in a,b) the reduced state and c,d) oxidized state after 20 redox cycles at 800 °C. The edge (outer surface) of the foams is marked with a white dashed line.

accumulation of vacancy during redox cycling increases microporosity within lamellae significantly, thus degrading the lamellar structure and leading to macroscopic foam swelling. This structural degradation is also reported in pure Fe, Fe—Ni, and Cu—Ni microparticles during high-temperature redox cycling.[23,53] Mitigating such porosity generation to stabilize lamellar structures may lead to further improvements in long-term redox cycling capability.

3. Conclusion

Our study investigates the role of tungsten in enhancing the sintering resistance of Fe-W foams with hierarchical porous structures during redox cycling. The W concentration in freeze-cast, lamellar Fe-W foams was varied from 10 to 33 at.% to achieve a broad range of Fe/Fe_2W phase fractions and to investigate associated effects on the reaction performance and structural evolution

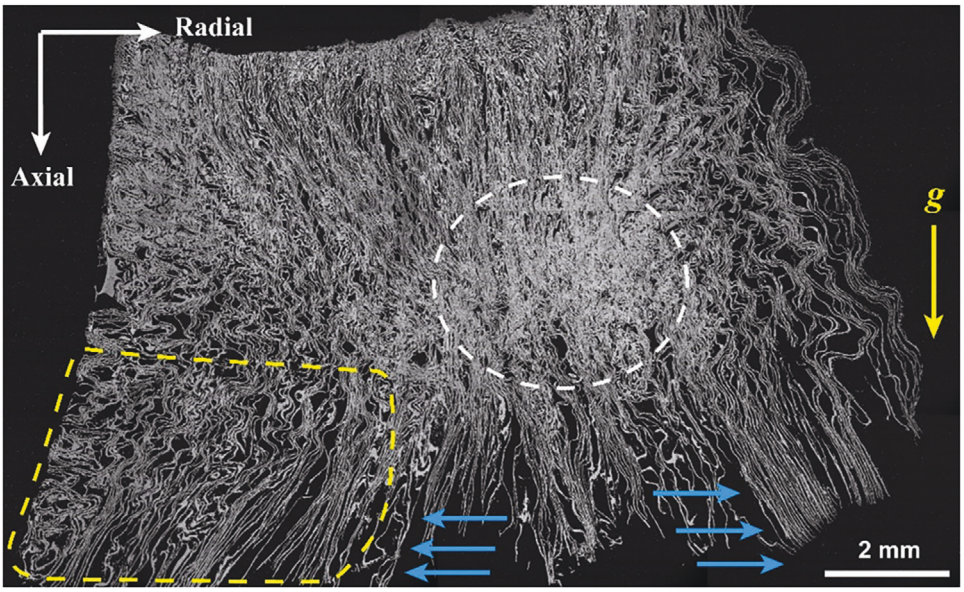

Figure 12. Stitched BSE micrographs of an axial cross-section of a full Fe-18 W foams after 20 redox cycles showing lamellar buckling (e.g., within the yellow dotted frame and partial densification (white dotted ellipse). The yellow vertical arrow indicates the direction of gravity g) during redox cycling. The blue horizontal arrows indicate the deflection of buckled lamellae in the radial direction due to brooming deformation.

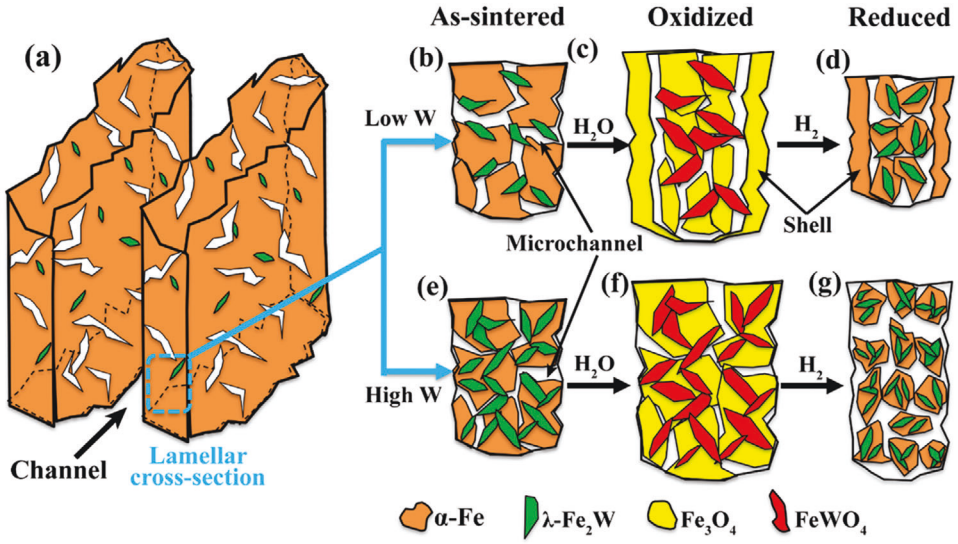

Figure 13. Schematic illustrating evolution processes during redox cycling for lamellar Fe-W foams with (b–d) low W and (e–f) high W content. The white region within the lamellae represents micro-porosity from freeze casting and partial sintering. Colored regions represent different phases: α-Fe in orange, λ-Fe_2W in green, $FeWO_4$ in red, and Fe_3O_4 in yellow. a) 3D view of two lamellae in an as-sintered foam. A magnified view of the cross-section of low-W lamellae is shown in the following panels: b) Initial microstructure showing uniform mixture of α-Fe and λ-Fe_2W phases in as-sintered lamella with microchannels; c) Core-shell structure, with dense Fe_3O_4 shell and porous core (comprising Fe_3O_4 and $FeWO_4$ phases) in the oxidized state; d) Metallic core-shell structure with dense α-Fe shell and porous α-Fe+λ-Fe_2W core in the reduced state. A magnified view of the cross-section of high-W lamellae is shown in the following panels: e) Initial microstructure of as-sintered lamella showing microchannels and ligaments with an uniform mixture of α-Fe and λ-Fe_2W phases; f) ligaments showing a homogeneous distribution of Fe_3O_4 and $FeWO_4$ phases; g) refined, uniform mixture of α-Fe+λ-Fe_2W phases in ligaments in the reduced state.

of foams during redox H_2/H_2O cycling at 800 ^{0}C. The following conclusions are reached:

1) Increasing W concentration has a minor effect on the oxidation rate but significantly extends the initial reduction time in the first cycle due to the slower reduction of more stable $FeWO_4$, as compared to Fe_3O_4.
2) The chemical vapor transport (CVT) mechanism during reduction refines stable W-rich phases to a nanocrystalline scale, boosting the reaction kinetics of subsequent redox cycles. The reduction time could be adjusted by designing W concentrations and associated phase fractions of $FeWO_4$.
3) Higher W concentration enhances the degradation resistance of Fe-W lamellar foams during high-temperature redox cycling, resulting in a more stable lamellae structure.
   a) In Fe-10 W foam, sintering and densification of lamellar structures are notable via core-shell segregation after 20 redox cycles, similar to the degradation observed in Fe,[54] Fe-Co, Fe-Cu,[32] and Fe-Ni[35] foams. During oxidation, Fe atoms diffuse outwards – microscopically to the surface of lamellae and macroscopically to the surface of the foams – which leads to the sintering of neighboring buckled lamellae and reduction in gas permeability.
   b) In Fe-18 W and Fe-25 W foams, the W-rich phases increase in volume fraction and they are in contact with the Fe-rich phases as (i) λ-Fe_2W/α-Fe in the reduced state and (ii) $FeWO_4/Fe_3O_4$ in the oxidized state. These dual-phase microstructures in ligaments within lamellae prevent Fe out-diffusion and shell formation, even after 50 redox cycles.
   c) Although increasing W concentration from 10 to 18 at.% enhances the stability of the lamellar structure effectively in Fe-W foams, lamellar buckling still occurs in Fe-18 W foam, inducing swelling of foams after 50 cycles.
4) Our work establishes a compositional window for designing Fe-W foams with high degradation resistance for long-term redox cycling for energy storage.

4. Experimental Section

Freeze Casting, Reduction, and Sintering of Fe-W Foams: Fe-W foams with four compositions, i.e., Fe-10 W, Fe-18 W, Fe-25 W, and Fe-33 W (at%), were prepared by freeze-casting of aqueous suspensions, ice sublimation, hydrogen reduction, and sintering, via methods previously reported for Fe foams[55–58] and Fe-based foams (Fe-Ni,[25,33,34] Fe-Co, Fe-Cu,[32] Fe-Mo).[40] In brief, aqueous suspensions were prepared by mixing Fe_2O_3 powders (Noah Technologies, 99.9%, <3 µm), WO_3 nanopowders (SS-Nano, 99.5%, <100 nm), DI water, and Zephrym PD 4974 (Croda) as a dispersant. Volume fractions of precursors in suspensions for various Fe-W foams are listed in Table 1. The suspensions were milled with yttria-stabilized zirconia milling balls for 24 h on a roller mixer. After milling, 2.0 vol% polyethylene glycol (PEG, M_n = 3350, Sigma–Aldrich) was added as a binder. The suspensions were vortexed for 2 min and then degassed and cooled in an ice-water bath (≈0 °C).

Directional freeze-casting was performed on a copper plate cooled by a thermoelectric chiller (Mauser Electronics). The suspensions were poured into a hollow Teflon mold (outer diameter: 25 mm, inner diameter: 15 mm, height: 15 mm) placed on the copper plate. The plate was then cooled to -30 °C following an exponential cooling function, so as to initiate ice growth at a constant rate from the bottom to the top of the mold. This results in ice dendrites with constant thickness and spacing throughout the height of freeze-casted foams.[28] After demolding, a 1–2 mm high section at the

bottom of the frozen specimen was cut and discarded. The cast specimens were placed in a freeze drier at a temperature of −54 °C under vacuum (≈13 Pa) for 24 h to sublimate the ice completely.

After ice removal, lamellar green bodies were thermally treated to achieve metallic foams in three steps under ultra-high purity (UHP) H_2 (Airgas) flow: i) debinding at 300 °C for 1 h to burn out all organic components; ii) reduction of Fe_2O_3 and WO_3 at 600 °C for 4 h; iii) sintering at higher temperatures for various time, depending on W concentrations, to partially densify lamellae. For the four Fe-W foams, thermal profiles of the debinding and reduction steps and cooling rates (10 °C min^{-1}) were the same, while temperatures and times for sintering (listed in Table 1) were varied to achieve similar porosities in foams with different compositions. The morphologies of as-sintered Fe-W foams with various W concentrations are shown in Figure S5 (Supporting Information).

Redox Cycling of Foams: Redox cycling of metallic foams was conducted in an alumina tube furnace (outer diameter: 25 mm, inner diameter: 20 mm, length: 500 mm) at 800 °C under flowing steam or UHP H_2. During the oxidation process, steam was supplied by flowing UHP Ar (Airgas) at 120 sccm, controlled by a mass flow controller (MKS Instruments), through a water bubbler heated to 93 °C to achieve an H_2O partial pressure of 77 kPa, enabling oxidization of Fe into Fe_3O_4 rather than Fe_2O_3.[59] During the reduction process, UHP H_2 was supplied at 200 sccm directly by another mass flow controller. A single redox cycle consists of both oxidation and reduction processes, a duration of 90 min for each, ensuring complete redox reactions (100% Fe utilization). After redox cycling, specimens were cooled to ambient temperature within the tube furnace by flowing either 20 sccm Ar-4% H_2 gas for oxidized foams or 100 sccm H_2 for reduced foams.

Microstructure Characterization: Foams were cold mounted with epoxy resin (Epothin 2 Resin, Buehler), vacuum infiltrated to fill porous structures, cured for 24 h, and polished with diamond suspensions (MetaDi, Buehler) down to 0.25 µm. For metallic foams in their reduced state, oil-based suspensions were used to avoid corrosion during polishing. Specimens were coated with a 6 nm thick osmium conductive layer and examined by scanning electron microscopy (SEM) using a Quanta 650 ESEM (ThermoFisher Scientific) instrument equipped with an Oxford Aztec Energy dispersive X-ray spectroscopy (EDS).

The surface area of as-sintered Fe-10 W, Fe-18 W, and Fe-25 W foams was measured by the Brunauer-Emmett-Teller (BET) method via nitrogen adsorption at −196 °C, using a Micromeritics 3-flex apparatus over a range of relative pressures (p/p°) from 0.05 to 0.30. Prior to analysis, foams were degassed for 8 h under vacuum in three steps: i) heating to 100 °C and holding for 1 h under vacuum to remove moisture and volatile impurities; ii) heating to 200 °C and holding for 2 h to eliminate any remaining moisture and adsorbed gases; iii) heating to 300 °C and holding for 4 h to remove strongly adsorbed impurities.

X-Ray Diffraction Characterization: In situ X-ray diffraction (XRD) was performed on freeze-cast Fe-W foams to characterize phase evolution during redox cycling in a modified Stadi-MP (Stoe, Germany) instrument[35,40,42] equipped with an asymmetric curved Ge monochromator under pure Ag-Kα1 radiation (λ = 0.56 Å) and a 1D silicon strip-detector (MYTHEN2 1k, from Dectris, Switzerland), operated at 40 kV and 40 mA (beam size: 4 × 0.8 mm). XRD patterns were collected in Debye–Scherrer transmission geometry, using 1 min scans with 2θ diffraction angles spanning 5.7–24.3°, after calibration against a NIST Si standard (640d).

A colony of lamellae was cut from Fe-10 W, Fe-18 W, and Fe-33 W foams in the as-sintered state, with a size of ≈1–1.5 mm in height and ≈1–1.5 mm in thickness. The specimen was then transferred into a quartz capillary (with an inner diameter of 1.5 mm) and surrounded on both ends by amorphous quartz wool to fix their position. The remainder of the capillary volume, on the inlet and outlet end of the sample, was filled with porous ceramic blocks to prevent sample movement upon changes in gas flow. The capillary was inserted into a water-cooled, graphite-heated furnace, with a temperature stability of 0.1 °C.

The samples were first heated to 800 °C (heating rate of 30 °C min^{-1}) under flowing Ar-4% H_2 to prevent oxidation prior to redox cycling. After reaching 800 °C, the gas was switched to UHP Ar, and bubbled through a 40 °C water bubbler for oxidation (P_{H2O} = 7.3 kPa). The gas lines between the bubbler and capillary were heated to >100 °C to prevent steam condensation. After complete oxidation, noted by unchanging diffraction patterns, the gas flow was switched to Ar-4% H_2 (flow rate of 60 sccm) for reduction. This diluted gas slowed the reduction reaction to match the time resolution of the collection of XRD patterns.

The measured XRD data were analyzed in MATLAB to plot the evolution of XRD patterns as a function of time after background correction with a modified polynomial fit. To study the evolution of each phase as a function of time, the strongest diffraction peaks (i.e., (1 1 0) reflection for α-Fe, (1 0 3) reflection for λ-Fe_2W, (1 −2 0) reflection for µ-Fe_7W_6, (1 1 3) reflection for Fe_3O_4, and (1 1 1) reflection for $FeWO_4$, indexed using reference patterns from the Inorganic Crystal Structure Database (ICSD)) were fitted with a Lorentzian function. These fitted peaks were then integrated to calculate their area and then normalized by the respective maximum value.

Ex situ XRD patterns of samples were measured in a reflection mode with pure Cu Kα1 radiation (λ = 1.54 Å) with a Rigaku Smartlab 3 kW Gen2. The reflection 2θ angles were scanned in a range of 25°–60° at a scanning speed of 2° min^{-1}.

Supporting Information

Supporting Information is available from the Wiley Online Library or from the author.

Acknowledgements

This research received financial support from the US National Science Foundation (CMMI-2015641). The work made use of the J.B. Cohen X-Ray Diffraction Facility supported by the MRSEC program via the National Science Foundation (DMR-2308691) at the Materials Research Center of Northwestern University and the Soft and Hybrid Nanotechnology Experimental (SHyNE) Resource (NSF ECCS-1542205) and the IMSERC X-Ray facility, which has received support from the Soft and Hybrid Nanotechnology Experimental (SHyNE) Resource (NSF ECCS-2025633), and Northwestern University (NU). This work also made use of the EPIC facility of Northwestern University's NUANCE Center, which has received support from the Soft and Hybrid Nanotechnology Experimental (SHyNE) Resource (NSF ECCS-1542205); the MRSEC program (NSF DMR-1720139) at the Materials Research Center; the International Institute for Nanotechnology (IIN); the Keck Foundation; and the State of Illinois, through the IIN. MC thanks Dr. Vinita Dubey and Dr. Neil M. Schweitzer for their help with the Brunauer-Emmett-Teller (BET) measurements.

Conflict of Interest

DCD discloses a financial interest in CellMobility, Inc. which commercializes freeze-cast metal foams. DCD and SMP disclose a patent application for "Refractory Alloyed Iron-based redox active foams for Iron-Air Batteries", U.S. Provisional Patent Application No. 63/406 320, and "Iron-Tungsten Redox System and Applications of Same", U.S. Provisional Patent Application No. 63/619.401.

Data Availability Statement

The data that support the findings of this study are available from the corresponding author upon reasonable request.

Keywords

degradation resistance, Fe-W foams, freeze casting, lamellar structures, redox cycling

Received: June 24, 2024
Revised: August 8, 2024
Published online:

[1] W. Zhang, J. Zhang, Q. Li, Y. He, B. Tang, M. Li, Z. Zhang, Z. Zou, In *Pro. of the 8th Pacific Rim Int. Congress on Advanced Materials and Processing*, Springer, Berlin, Heidelberg **2013**, 777.
[2] D. Spreitzer, J. Schenk, *Reduction of Iron Oxides with Hydrogen—A Review*, Vol. *90*, Wiley-VCH, Verlag **2019**.
[3] P. Debiagi, R. C. Rocha, A. Scholtissek, J. Janicka, C. Hasse, *Renewable Sustainable Energy Rev.* **2022**, *165*, 112579.
[4] C. M. Berger, O. Tokariev, P. Orzessek, A. Hospach, Q. Fang, M. Bram, W. J. Quadakkers, N. H. Menzler, H. P. Buchkremer, *J. Energy Storage* **2015**, *1*, 54.
[5] W. W. Drenckhahn, H. Greiner, M. Kühne, H. Landes, A. Leonide, K. Litzinger, C. Lu, C. Schuh, J. Shull, T. Soller, *ECS Trans.* **2013**, *50*, 125.
[6] S. Trocino, M. Lo Faro, S. C. Zignani, V. Antonucci, A. S. Aricò, *Appl. Energy* **2019**, *233–234*, 386.
[7] Q. Fang, C. M. Berger, N. H. Menzler, M. Bram, L. Blum, *J. Power Sources* **2016**, *336*, 91.
[8] L. Zeng, Z. Cheng, J. A. Fan, L.-S. Fan, J. Gong, *Nat Rev Chem* **2018**, *2*, 349.
[9] T. Mattisson, A. Lyngfelt, P. Cho, *Fuel* **2001**, *80*, 1953.
[10] A. Thursfield, A. Murugan, R. Franca, I. S. Metcalfe, *Energy Environ. Sci.* **2012**, *5*, 7421.
[11] I. S. Metcalfe, B. Ray, C. Dejoie, W. Hu, C. de Leeuwe, C. Dueso, F. R. García-García, C.-M. Mak, E. I. Papaioannou, C. R. Thompson, J. S. O. Evans, *Nat. Chem.* **2019**, *11*, 638.
[12] S. Wang, G. Wang, F. Jiang, M. Luo, H. Li, *Energy Environ. Sci.* **2010**, *3*, 1353.
[13] J. J. Wong, D. Iruretagoyena, N. Shah, P. S. Fennell, in Proc. of the Royal Society A: Mathematical, Physical and Engineering Sciences, Royal Society, London **2023**, 479.
[14] V. Galvita, T. Hempel, H. Lorenz, L. K. Rihko-Struckmann, K. Sundmacher, *Ind. Eng. Chem. Res.* **2008**, *47*, 303.
[15] N. V. R. A. Dharanipragada, L. C. Buelens, H. Poelman, E. De Grave, V. V. Galvita, G. B. Marin, *J Mater Chem A Mater* **2015**, *3*, 16251.
[16] M. Bui, C. S. Adjiman, A. Bardow, E. J. Anthony, A. Boston, S. Brown, P. S. Fennell, S. Fuss, A. Galindo, L. A. Hackett, J. P. Hallett, H. J. Herzog, G. Jackson, J. Kemper, S. Krevor, G. C. Maitland, M. Matuszewski, I. S. Metcalfe, C. Petit, G. Puxty, J. Reimer, D. M. Reiner, E. S. Rubin, S. A. Scott, N. Shah, B. Smit, J. P. M. Trusler, P. Webley, J. Wilcox, N. M. Dowell, *Energy Environ. Sci.* **2018**, *11*, 1062.
[17] M. E. Gálvez, P. G. Loutzenhiser, I. Hischier, A. Steinfeld, *Energy Fuels* **2008**, *22*, 3544.
[18] J. J. Morales Corona, K. Sedransk Campbell, P. S. Fennell, *Greenhouse Gases: Sci. Technol.* **2023**, *13*, 565.
[19] C. Zhang, K. Huang, *ACS Energy Lett.* **2016**, *1*, 1206.
[20] X. Zhao, Y. Gong, X. Li, N. Xu, K. Huang, *J. Electrochem. Soc.* **2013**, *160*, A1241.
[21] Q. Zafar, T. Mattisson, B. Gevert, *Energy Fuels* **2006**, *20*, 34.
[22] S. Ma, S. Chen, A. Soomro, W. Xiang, *Energy Fuels* **2017**, *31*, 8001.
[23] C. Chung, L. Qin, V. Shah, L.-S. Fan, *Energy Environ. Sci.* **2017**, *10*, 2318.
[24] J. A. Carpenter, Z. Saraw, A. Schwegler, T. Magrini, G. Kuhn, A. Rafsanjani, A. R. Studart, *Adv. Mater.* **2023**, *35*, 2207181.
[25] S. M. Pennell, B. Chappuis, J. A. Carpenter, D. C. Dunand, *Adv. Funct. Mater.* **2023**, *33*, 2307470.
[26] S. Deville, *Adv. Eng. Mater.* **2008**, *10*, 155.
[27] A. M. Anderson, M. G. Worster, *Langmuir* **2012**, *28*, 16512.
[28] C. Stolze, T. Janoschka, U. S. Schubert, F. A. Müller, S. Flauder, *Adv. Eng. Mater.* **2016**, *18*, 111.
[29] K. L. Scotti, D. C. Dunand, *Prog. Mater. Sci.* **2018**, *94*, 243.
[30] U. G. K. Wegst, P. H. Kamm, K. Yin, F. García-Moreno, *Nat. Rev. Methods Primer* **2024**, *4*, 28.
[31] A. A. Plunk, D. C. Dunand, *Mater. Lett.* **2017**, *191*, 112.
[32] S. M. Pennell, J. B. Mack, D. C. Dunand, *J. Alloys Compd.* **2022**, *918*, 165606.
[33] S. K. Wilke, J. B. Mack, C. Kenel, D. C. Dunand, *J. Alloys Compd.* **2022**, 889.
[34] S. K. Wilke, D. C. Dunand, *J. Mater. Chem. A Mater.* **2020**, *8*, 19375.
[35] J. B. Mack, S. M. Pennell, D. C. Dunand, *Acta Mater.* **2022**, *237*, 118148.
[36] M. Hasegawa, In *Treatise on Process Metallurgy*, Elsevier, Amsterdam, Netherlands **2013**, 507.
[37] A. Ruiz Puigdollers, P. Schlexer, S. Tosoni, G. Pacchioni, *ACS Catal.* **2017**, *7*, 6493.
[38] B. de Caprariis, M. Damizia, P. De Filippis, M. P. Bracciale, *Int. J. Hydrogen Energy* **2021**, *46*, 39067.
[39] K. Otsuka, T. Kaburagi, C. Yamada, S. Takenaka, *J. Power Sources* **2003**, *122*, 111.
[40] J. B. Mack, S. M. Pennell, D. C. Dunand, *Acta Mater.* **2023**, *254*, 119015.
[41] W. V. Schulmeyer, H. M. Ortner, *Int J Refract Metals Hard Mater* **2002**, *20*, 261.
[42] S. Pennell, M. Chen, D. C. Dunand, *Small* **2024**.
[43] S. Pennell, D. C. Dunand, *Scr. Mater.* **2024**, *249*, 116177.
[44] A. K. Sinha, W. Hume-Rothery, IRON–TUNGSTEN SYSTEM.. United Kingdom: N. p., 1967. Web.
[45] N. Asrar, L. L. Meshkov, E. M. Sokolovskaya, *J. Less-Common Met.* **1988**, *144*, 41.
[46] S.-H. Kim, X. Zhang, Y. Ma, I. R. Souza Filho, K. Schweinar, K. Angenendt, D. Vogel, L. T. Stephenson, A. A. El-Zoka, J. R. Mianroodi, M. Rohwerder, B. Gault, D. Raabe, *Acta Mater.* **2021**, *212*, 116933.
[47] J.-R. Gavarri, C. Carel, *Prog. Solid State Chem.* **2019**, *53*, 27.
[48] J. A. Bustnes, *Metall. Mater. Trans. B.* **1997**, *28*, 613.
[49] X. WU, J. LUO, B. LU, C. XIE, Z. PI, M. HU, T. XU, G. WU, Z. YU, D. YI, *Trans. Nonferrous Met. Soc. China.* **2009**, *19*, s785.
[50] G. A. Greene, C. C. Finfrock, *Exp. Therm. Fluid. Sci.* **2001**, *25*, 87.
[51] B. D. Cullity, *Elements of X-ray Diffraction*, Addison-Wesley Publishing, Boston, Massachusetts, USA **2014**.
[52] R. Morales, D. Sichen, S. Seetharaman, I. Arvanitidis, *Metall. Mater. Trans. B.* **2002**, *33*, 589.
[53] L. Qin, A. Majumder, J. A. Fan, D. Kopechek, L.-S. Fan, *J. Mater. Chem. A* **2014**, *2*, 17511.
[54] S. K. Wilke, D. C. Dunand, *Acta Mater.* **2019**, *162*, 90.
[55] S. K. Wilke, D. C. Dunand, *Acta Mater.* **2019**, *162*, 90.
[56] S. K. Wilke, R. A. Lundberg, D. C. Dunand, *ACS Appl. Mater. Interfaces* **2020**, *12*, 27190.
[57] S. K. Wilke, D. C. Dunand, *J. Power Sources* **2020**, *448*, 227463.
[58] S. Pennell, D. Dunand, *Acta Mater.* **2023**, *243*, 118543.
[59] I. G. Wright, R. B. Dooley, A review of the oxidation behaviour of structural alloys in steam, Vol. *55*, pp. 129–167.